

Influence of the microstructure on mechanical properties of SLM additive manufacturing Fe-based bulk metallic glasses

Qi Jiang^{a,b}, Peilei Zhang^{a,b,c*}, Jie Tan^{a,b}, Zhishui Yu^{a,b*}, Yingtao Tian^d, Songyun Ma^e, Di Wu^{a,b}

^aSchool of Materials Engineering, Shanghai University of Engineering Science, Shanghai 201620, China

^bShanghai Collaborative Innovation Center of Laser of Manufacturing Technology, Shanghai 201620, China

^cFraunhofer Institute for Laser Technology ILT, Aachen 52074, Germany

^dDepartment of Engineering, Lancaster University, Lancaster LA1 4YW, United Kingdom

^eInstitute of General Mechanics, RWTH Aachen University, Aachen 52062, Germany

Abstract:

Fe-based bulk metallic glass (BMG)(FeCrMoWMnSiBC) was produced by selective laser melting (SLM) successfully in this study. The best parameters were determined through extensive experiments. The relative density (95%) and amorphous rate (95.47%) samples were obtained by this parameter. The analysis of the microstructure reveals that the crystalline phases in the heat affected zone (HAZ) are mainly α -Fe and $M_{23}(CB)_6$ phases, and co-exist with the amorphous phases. The Heat treatment is employed to study the crystallization behavior of amorphous phases. The α -Fe phase, as the primary phase, grows into a submicron crystal phase under the action of multiple thermal cycles. Nanoindentation test results show that the hardness of the amorphous phase is higher than that of the nano-grain region, and the hardness of the nanocrystalline region is higher than that of the submicron-grain region. The free volume content is different and the amorphous phase is not uniform due to the complex thermal cycle. The maximum hardness occurs in the amorphous phase with 22.6 GPa.

Keywords: Bulk metallic glass; Selective laser melting; Crystallization; Annealing

* Corresponding authors: Peilei Zhang (peilei@sues.edu.cn) and Zhishui Yu (yu_zhishui@163.com)

1. Introduction

Bulk metallic glass (BMG) has better mechanical, physical and chemical properties than conventional alloys [1–3]. The excellent physical and chemical properties of amorphous alloys have attracted the attention of a large number of researchers [4]. Nowadays, various systems of amorphous alloys are appearing in front of people, such as Zr-based [5], Ni-based [6], Al-based [7], Ti-based [8,9] and Fe-based [10,11] amorphous alloys, etc. The researchers have produced the amorphous alloys by casting and melt spinning, in the early studies [4]. However, the cooling rate of the traditional production method is limited, which can only satisfy the production of a small number of amorphous alloys with a great amorphous forming ability [2]. But with the development of industry, the structure of components becomes more and more complex. In order to meet the industrial application of BMG alloys, the traditional manufacturing method is difficult to meet the requirements of industry [12]. The development of Additive Manufacturing (AM) technology can be a good solution to this problem. AM technology is a production method in which the part model is sliced by CAD software and then printed layer by layer [13]. Thus, the AM production method can accommodate complex parts. SLM technology as a type of AM technology has a higher cooling rate compared to traditional copper casting ($10^2\sim 10^{13}$ K/s), making SLM technology ideal for BMG production [11,14].

So far, there are many studies on BMG printing via SLM. In the study of Li et al. [15], it was found that the phase distribution within the sample could be controlled by adjusting the process parameters, which improved the mechanical properties of the specimen. The differences in the amorphous microstructure of Zr-based produced by SLM were investigated by Ouyang et al. [16]. By studying the amorphous phases at different locations, it was found that the differences in the amorphous phases were mainly influenced by the crystalline phase. In the simulation of the amorphous SLM production process, it was found that there were gradients in the microstructure of the amorphous specimen due to the presence of cyclic thermal cycling [10]. In a comparative study of Zr-based amorphous via casting and SLM-produced specimens, Pacheco et al. [17] found that the SLM-produced specimens had a greater tendency to crystallize. Nowadays, the Fe-based amorphous has become a hot research topic due to its excellent soft magnetic properties, mechanical properties, low damping factor and low material cost [18]. However, the low glass forming ability of Fe-based amorphous makes it inevitable to produce crystalline phases during SLM production [19]. Finite element analysis of SLM for the production of Fe-based amorphous found that sufficiently high cooling rate, short exposure time at high temperature and good thermal stability are key factors for the production of BMG with a low crystallization rate by wang et al. Luo et al. [20] produced Fe-based amorphous specimens by snake-shaped line scanning combination with alternating transformations between adjacent layers. It was found that the microstructure

1 transition from crystalline to almost completely amorphous when the laser power was reduced or the scanning speed
2 was increased to reduce the energy density. In a study by Wang et al. [11] it was pointed out that when the temperature
3 of the heat affected zone (HAZ) is higher than the crystallization temperature of the amorphous alloy, it theoretically
4 causes the generation of crystalline phases. It was found that when the temperature in the HAZ exceeds the
5 crystallization temperature it does not necessarily lead to the production of crystalline phases, they believe that a
6 latency period of almost 1.87ms is also required. A different view was presented by Mahbooba et al. [3] who argued
7 that stress-induced crystallization is the main cause of crystalline phase generation. In the study of Li et al. [21] the
8 presence of contaminants was proposed as the main cause of crystallization. As we know, the formation of the
9 crystalline phase will reduce the mechanical and physical properties of amorphous materials[22]. But there are few
10 studies on the effect of different crystalline phases on the properties of Fe-based amorphous alloys made by SLM.
11 Besides, the researchers have made great efforts to realize the industrial application of Fe-based amorphous. In 2013,
12 IFW was the first to report that the Fe-based bulk metallic glass was formed by SLM and successfully manufactured
13 a 3D stent structure[23]. Yang et al. [24] produced structural parts of $Zr_{55}Cu_{30}Ni_5Al_{10}$ BMG by SLM. It was found
14 that after the dealloying treatment Cu^+ acted as a Fenton-like reagent, presenting an efficient catalytic effect on azo
15 compounds. As Fenton reagent, Fe^{2+} ion has a high catalytic effect on azo compounds. And there are few studies on
16 catalytic azo compounds for Fe-based amorphous structural components. This experiment explored the direction of
17 Fe-based amorphous structural components as catalysts.

18
19 In our previous work, we have studied in detail the laser additive manufacturing Fe-based metallic glass. For
20 example, we studied the crystal phase competition behavior of Fe-based metallic glass [25,26], and the stability of
21 the molten pool [27]. Meanwhile, the effect of annealing on Fe-based metals [28], and the composition design
22 principle of Fe-based BMG were studied [29]. The influence of the magnetic field on the forming of iron-based
23 metallic glass has also been studied [30]. These researches have laid a foundation for further research on laser additive
24 manufacturing of Fe-based BMG.

25
26 In the research of this paper, energy density was used as the criterion to judge the sample forming, and the
27 microstructure in the HAZ was studied. The microstructure of Fe-based BMGs at different energy densities was
28 investigated. Annealing treatment was used to analyze the crystallization process. The best formed specimens were
29 subjected to nanoindentation tests to analyze the reasons for the different mechanical properties. We have also
30 explored the degradation of azo dyes in Fe-based BMG structural parts.

2. Materials and methods

The samples were built with a commercial SLM facility (M2 Multilaser). The Fe-based amorphous powders with a size distribution of 15 to 53 μm were used. The nominal alloy composition was 16-19% Cr, 13-16% Mo, 5-7% W, 1.5-3% Mn, 1-2% Si, 2.4-4.5% B, and 0.5-1% C (all in wt.%) and the balance was Fe. The samples were printed on the steel substrate with the island scanning strategy (As shown in Fig.1), and the substrate was preheated to 160 $^{\circ}\text{C}$ before printing. The printed sample with the dimension of 10*10*10mm³. The printing process was under argon atmosphere protection. The process parameters of sample printing vary the laser power (60-420W) and scanning speed (1200-3400mm/s) at the scanning spacing of 95 μm and layer thickness of 30 μm . The energy density can be obtained according to Eq. (1)[31]:

$$E = \frac{p}{vth} \quad (1)$$

where E, p, v, t, and h were energy density, laser power, scanning speed, layer thickness, and scanning hatch.

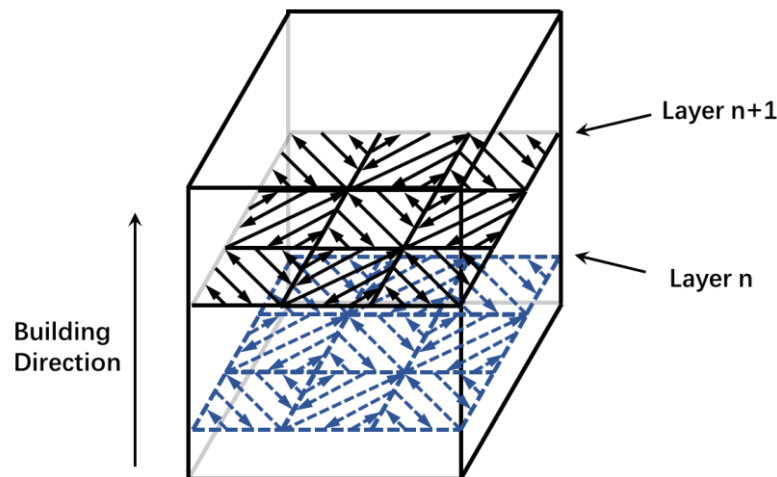


Fig.1 The scanning strategy of island

The microstructure of as-printed samples was characterized by microscope (Keyence, VHX-5000) and SEM (TESCAN 3400). The powder and as-printed samples were analyzed by X-ray diffraction (XRD, X'Pert Pro). The thermal stability was analyzed by differential scanning calorimeter (DSC, STA 2500) and the heating rate was 20 k/min. Transmission electron microscopy (TEM) was used to further analyze the crystalline phase. The heat treatment was carried out in a vacuum heat treatment furnace, and different heat treatment temperatures were determined according to the DSC crystallization curve. The heat-treated samples were kept in the furnace for two hours and then cooled with the furnace. Nano-indentation test was used to express micro-mechanical properties by Nano Indenter G200 (Keysight). The sample was dealloyed with H₂SO₄ (1mol/L), and the treatment time was 6h. The methyl orange

(20mg/L) was prepared as the raw material for degradation, and the samples treated with and without dealloying were placed in it and stood for 30 minutes at room temperature to observe the decolorization degree.

3. Result and Discussion

3.1 Macrostructure

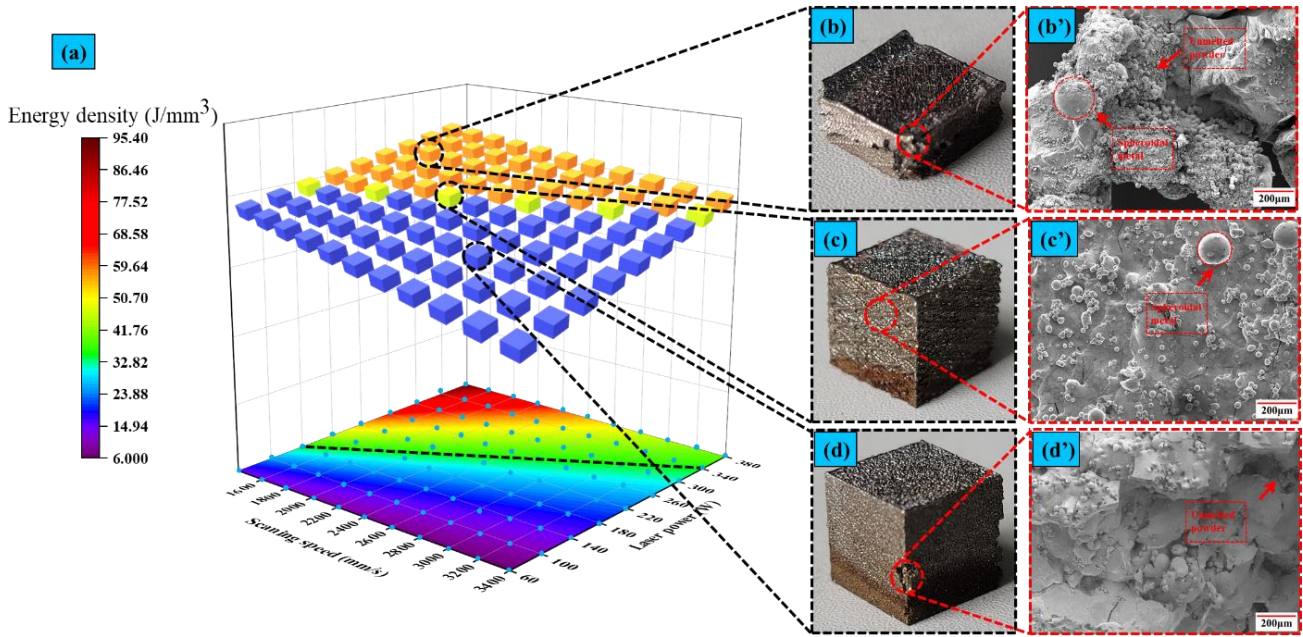


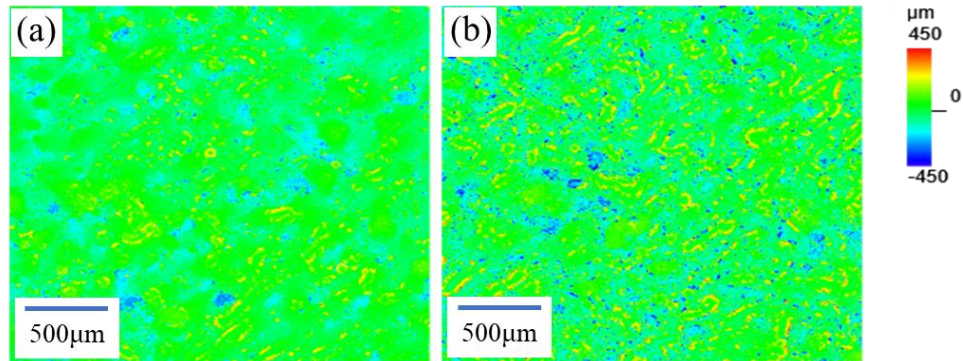
Fig. 2 The as-printed samples (a) The printed energy density distribution of specimens (b) The formed specimens with the energy density of 65.79 J/mm³ (c) The formed specimens with the energy density of 35.1 J/mm³ (d) The formed specimens with the energy density of 17.54 J/mm³ (b') The magnification of the warped edge of sample b (c') The magnification of the side of sample c (d') The magnification of the exfoliation of sample d.

Fig. 2 (a) shows the energy density distribution of the specimens at different process parameters. The forming of the specimens can be divided into three parts according to the energy density of 35.1 J/mm³. The maximum energy density of the sample is 95.24 J/mm³ (P=380W, V=1400mm/s), and the minimum is 6.19J/mm³ (P=60W, V=3400mm/s). In Fig. 2 (a), the orange square represents the sample with an energy density greater than 35.1 J/mm³, the blue square represents the sample with an energy density lower than 35.1 J/mm³, and the cyan square represents the sample with an energy density of 35.1 J/mm³. The Fig. 3 shows the surface roughness of specimens with energy densities of 35.1 J/mm³(Fig. 2(c)) and 17.54 J/mm³(Fig. 2(d)) respectively.

The Fig. 2 (b) was shown the sample with the energy density of 65.79 J/mm³, where the specimen clearly failed.

1 The energy density of the printed specimen is too high resulting in a high melt pool temperature and a large volume
2 expansion of the liquid metal. When the liquid metal solidifies, the volume of the melt pool shrinks drastically[32].
3
4 Meanwhile, the high scanning speeds during SLM printing can cause instability in the melt pool and melt pool
5 breakage. This phenomenon is known as Plateau Rayleigh instability[33], and the broken melt pool tends to coalesce
6 under the influence of the Marangoni effect, resulting in edge spherulite [34]. There is a large amount of free-flowing
7 powder on the edge of the sample, which will exacerbate the phenomenon of spherulite. The spherical metal is not
8 strong in combination with the layer of the printing. Under the action of high energy density, more metals could be
9 melted by the laser, which will produce greater internal stress during the rapid cooling process[4,35]. As the number
10 of printing layers increases, the internal stress is constantly accumulating, which aggravates the curl phenomenon at
11 the sample edge, and the specimen fails to print. Fig. 2(b') shows the back of the dotted circle in Fig. 2(b), which
12 proves the above inference that there is spherical metal and a large amount of unmelted powder at the corners. In
13 addition, when the energy density used for printing the sample is too high, the amorphous rate inside the sample will
14 be reduced[15]. The specific implications will be analyzed in the next section. It is found that when the energy density
15 is 35.1 J/mm³, the sample is on the boundary between formed and unformed. As shown in Fig. 2(c), a ribbed structure
16 exists on the side of the sample. The shaping is unstable due to the energy density of 35.1 J/mm³ as a boundary. Fig.
17 2(c') is a locally enlarged image of the side of the sample in Fig. 2(c), it could be seen that the spherical metal exists
18 on the side. Due to the island scanning strategy adopted, there is a certain amount of heat accumulation on the edge
19 of each island[18]. However, due to the relatively high energy density of the specimen in Fig. 2(c), a more dense
20 upper surface is formed compared to the energy density of 17.5 J/mm³ (Fig. 2(d)) [36]. The unstable melt pool when
21 producing specimens at low energy densities results in uneven widths of each weld path. The low energy density
22 makes the temperature of the molten pool too low, which is difficult to spread the molten pool. The narrow and high
23 weld pass was formed, which will affect the stability of the next layer of printing[37]. In the study of Zakrzewski et
24 al. [38], it was pointed out that the surface roughness of the sample can be improved by appropriately increasing the
25 energy density. As shown in Fig. 3, when the energy density is low, the surface roughness of the sample changes
26 significantly, while when the energy density is 35.1 J/mm³, the surface of the sample is significantly smoother. The
27 results in Fig. 3 also prove this point. It can be seen from Fig. 2 (d) that the structure of the sample is loose and there
28 is a phenomenon of falling off at the corners. When the energy density is too low, the powder layer can't get enough
29 energy input, and the powder melting is not complete, forming the phenomenon of poor interparticle bonding[1,39].
30 As shown in Fig. 2(d'), when the energy density is 17.54 J/mm³, there is a large number of unmelted powder particles

1 inside the detached part of the printing sample, which indicates that the lack of energy density causes the looseness
2 of the overall structure[40].
3



18 Fig.3 The surface roughness of the specimen. (a) The surface of sample with the energy density of 35.1J/mm³ (b) The surface of
19 sample with the energy density of 17.54J/mm³.
20
21
22
23

24 3.2 Microstructure

25
26 Fig. 4 shows the microstructure of the parts produced at energy densities of 17.54 J/mm³, 35.1 J/mm³ and 65.79
27 J/mm³ respectively. As shown in Fig. 4(a)-(c), the HAZ in the sample is gradually obvious with the increase of energy
28 density. During the process of amorphous SLM additive manufacturing, the HAZ represents the region of
29 crystallization[17]. Therefore, it can be learned that the crystallization region was expanded as the energy density
30 increases. The cooling rate of the SLM additive manufacturing process is up to 10²-10¹³ K/s. Generally, the cooling
31 rate of SLM technology is greater than the critical cooling rate of most amorphous alloys[41]. Amorphous alloys are
32 often formed with large supercooling, where the Gibbs free energy in the liquid state (G_L) is greater than the Gibbs
33 free energy in the solid state (G_S) when the temperature is less than the theoretical crystallization temperature.
34 According to the formula $\Delta G = G_L - G_S$, it can be concluded that $\Delta G < 0$ for amorphous therefore the amorphous alloy
35 itself tends to spontaneously nucleate[16]. The laser is applied to the specimen and the large cooling rate of the melt
36 pool inhibits the formation of crystal nuclear, but the radiation and conduction of heat from the laser causes the
37 temperature of the HAZ to exceed the crystallization temperature (T_g) of the amorphous alloys [10,17]. The line scan
38 by energy spectrum in Fig. 4(d) shows that there is an uneven distribution of elements in the HAZ, with the element
39 of Fe showing a clear decrease and the elements of Cr and Mo showing a slight increase. According to the principle
40 of equilibrium solidification, $\Delta G < 0$ provides the driving force for crystallization, and under the influence of the
41 thermal cycle, elemental segregation and energy fluctuations are produced, and finally generate crystallization in the
42 HAZ[42]. While the reduction of the element Fe is abnormal. The curve from the line scan by energy spectrum was
43
44
45
46
47
48
49
50
51
52
53
54
55
56
57
58
59
60
61
62
63
64
65

shown that there was no tendency for a significant decrease of Fe in the amorphous region. The decrease of Fe is due to the formation of a crystalline phase which is susceptible to corrosion.

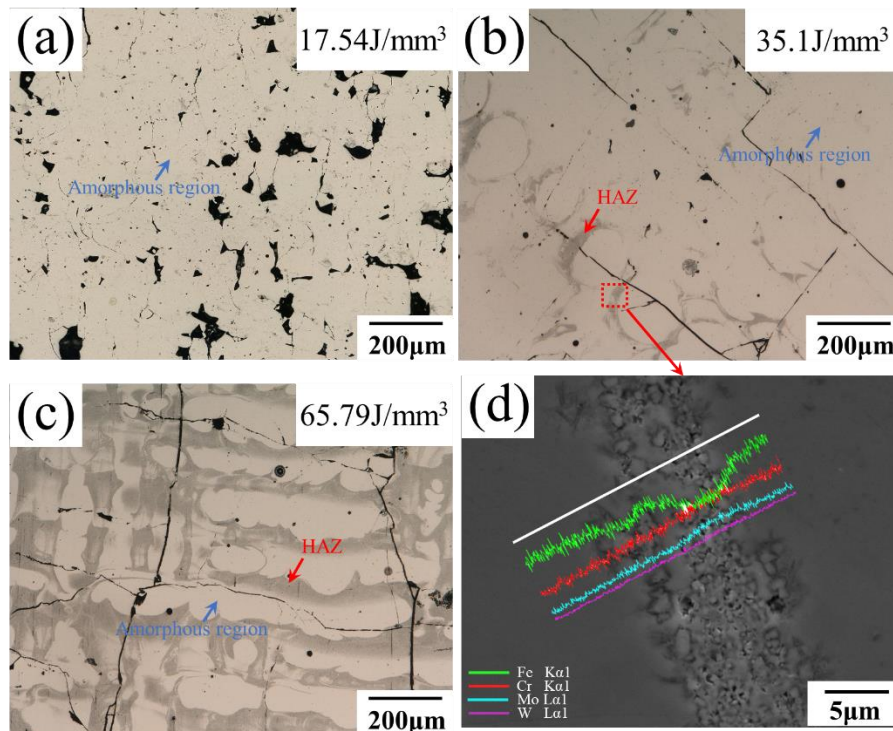


Fig. 4 Microstructure of samples: a) Microstructure of sample with the energy density of 17.54 J/mm³; b) Microstructure of sample with the energy density of 35.1 J/mm³; c) Microstructure of sample with the energy density of 65.79 J/mm³; d) Microstructure of HAZ and molten pool.

In addition, with the increase of energy density, the hole in the sample decreases obviously, but the crack increases. The increased energy density reduces the surface tension of the liquid melt pool, resulting in a better spread of the melt pool and a more continuous and regular weld path, as explained above. The high energy density also results in a higher temperature of the melt pool, which increases the time for porosity to escape during the printing process[5,43]. As shown in Fig. 4 (a-c), most of the cracks start at the junction between the HAZ and the amorphous region, where the cracks tend to sprout and expand due to the thermal stresses gather at the junction after a complex thermal cycle[9,39]. According to the free volume theory, even after the thermal cycle annealing treatment, there is still internal stress in the HAZ, which will increase the concentration of stress after crystallization, because the volume will change after crystallization of the sample, which increases the concentration effect of internal stress at the junction of the HAZ and the amorphous zone[2,44]. This is the reason why the cracks gradually become thick and occur at the junction of the HAZ and the amorphous zone with the increase of energy density.

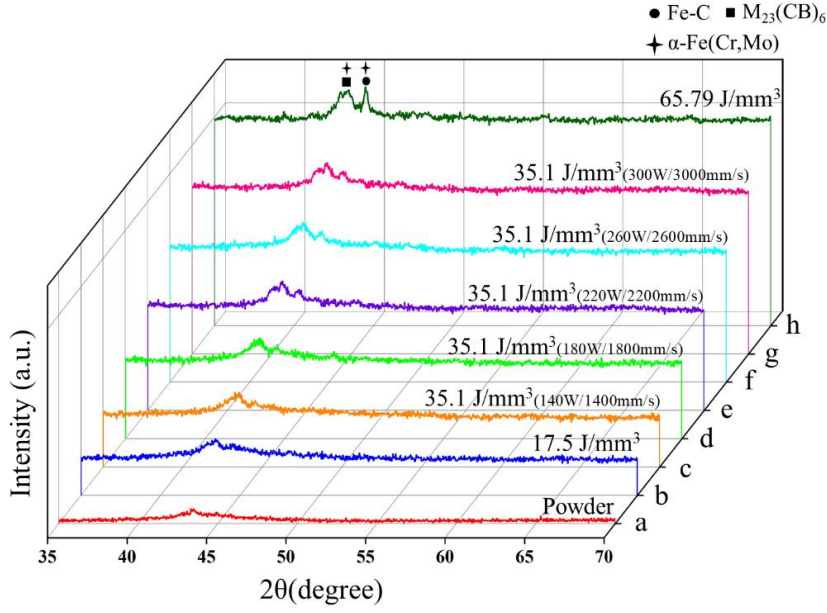


Fig. 5 XRD patterns: (a,b,f,h) XRD patterns at different energy densities. (c-g) XRD patterns of specimens with energy densities of 35.1J/mm³ were obtained by different process parameters.

As shown in Fig. 5, the XRD results show that the crystallinity of the specimen is mainly influenced by the energy density. When the energy density was less than 35.1 J/mm³, there was no obvious bragger peak in the XRD pattern. The bragger peak occurs at positions 42° and 44° when the energy density is 35.1 J/mm³. Due to the small grain size, there are no obvious bragger peaks at other locations. The bragger peak of 42° becomes more obvious at the energy density of 65.79 J/mm³. However, at an energy density of 35.1 J/mm³, there is no significant effect of different scan rates and laser powers on the bragger peaks. This phenomenon can be explained by Eq. (2). The Eq. (2) shows the relationship between the process parameters and the cooling rate [45] :

$$\frac{dT}{dt} = -2\pi k \left(\frac{V}{P}\right) \Delta T^2 \quad (2)$$

where k is the thermal conductivity, V is the scanning speed, P is laser power, and ΔT is the temperature difference during cooling. (The layer thickness is constant in the experiment, so the layer thickness is not considered). According to Eq. (2), the cooling rate is inversely proportional to the energy density. When the energy density is constant, the scanning speed varies in parallel with the laser power, so that different process parameters have less influence on the crystallization of the specimen. The main crystalline phases are α -Fe, $M_{23}(CB)_6$ and Fe-C through the analysis of XRD bragger peaks. These phases have proven to be common competing growth phases in the additive manufacturing of Fe-based amorphous alloys[46,47]. The α -Fe phase was often found in some amorphous

components with poor GFA. The α -Fe phase has a simple body-centered cube, which can be formed in the range of 1-2 nm. The formation of α -Fe nanocrystalline phases can be considered as the result of the aggregation of medium-range ordered (MRO) structures [48]. The $M_{23}(CB)_6$ phase has a complex icosahedral cluster structure that requires a long-range ordered structure in the melt pool to form. The formation of icosahedral clusters is usually preceded by the formation of metastable phases such as quasi-icosahedral structures or M3B (Fe3B) phases [49]. However, the molten pool cools extremely fast in the selective laser melting process. This is the reason why this crystalline phase is difficult to detect at low energy densities.

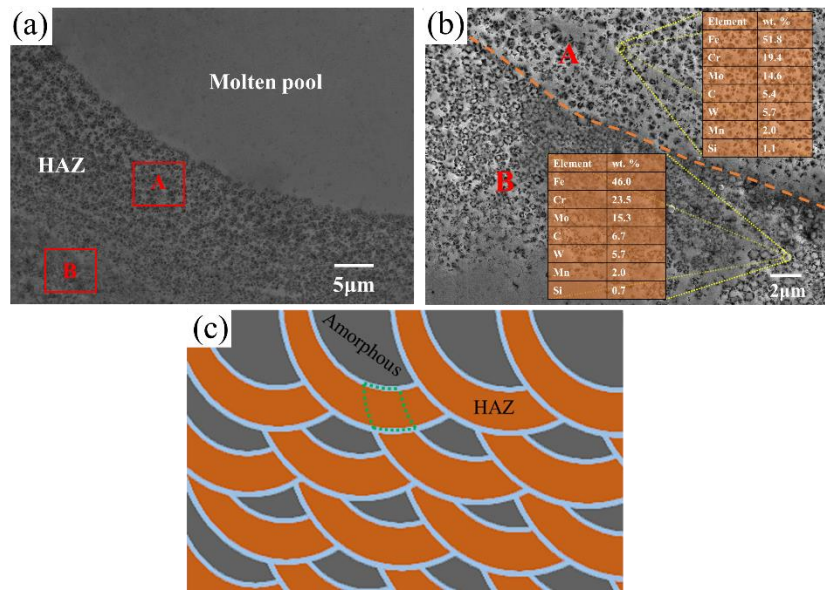


Fig. 6 The local enlargement of the HAZ of a specimen with an energy density of 35.1 J/mm³. (a) The SEM image of the molten pool and HAZ of a specimen with the energy density of 35.1 J/mm³. (b) The magnified view of HAZ. (c) The schematic diagram of microstructure arrangement

The magnification figure of the HAZ revealed a phenomenon that demonstrated the XRD results. There are obvious differences in the structure of the crystalline zone, as shown in Fig. 6. This has a significant difference from the HAZ structure shown in Fig. 4 (d). The Fig. 6 shows that the amorphous matrix is doped in both the crystalline zone A and B. The EDS scan results of region B indicate the crystallization phase is $M_{23}(BC)_6$ [50]. The EDS results of area A is shown the gathering of Fe elements and the content of C decreases. As shown in the XRD detection results in Fig. 5(f), the crystalline phases in the samples are mainly α -Fe phases. Therefore, it can be inferred that the crystalline phase in region A is α -Fe combined with the EDS results. There is a clear boundary between region A and region B, which has a similar shape to the fusion line. This indicates that the generation of submicron grains is related

to the thermal cycle. As shown in the green dashed box in Fig. 6 (c), the portion was heat treated by the temperature above T_g twice.[16]. When the heat treatment temperature is higher than T_g , $\Delta G < 0$ in the amorphous phase, combined with the internal stress generated after partial crystallization and the internal stress stored during the rapid solidification of the sample will become the driving force of crystallization[17]. In order to further analyze the composition of the HAZ, the TEM test results give more powerful proof.

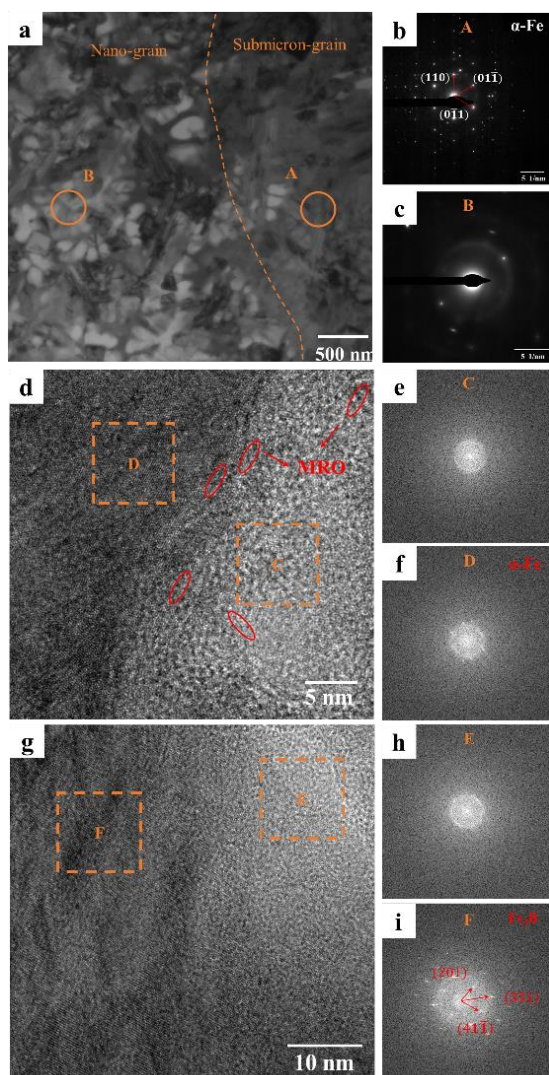


Fig. 7 (a)The TEM bright-field micrograph of HAZ. (b) the diffraction pattern of region A of Fig. 6a. (c) the diffraction pattern of region B of Fig. 6a. (d) the high magnifications bright-field image of α -Fe phase and amorphous. (e) the FFT image of region C of Fig. 6d. (f) the FFT image of region D of Fig. 6d. (g) the high magnifications bright-field image of Fe_3B phase and amorphous. (h) the FFT image of region E of Fig. 6g. (i) the FFT image of region F of Fig. 6g.

The different crystallization regions of TEM images were shown in Fig. 7. The nano-grain area (region A) and

1 the submicron-grain area (region B) could be seen in Fig. 7(a). The white phase is marked as amorphous in region B,
2 and there are some nanocrystals as shown in Fig. 7(c). In region A, the α -Fe phase could be confirmed and the
3 nanocrystal ring could be observed too. It can be further confirmed that α -Fe is the main competing crystalline phase.
4 Fig. 7(d) shows the interface between the crystalline phase (α -Fe) and the amorphous phase in the nanocrystalline
5 region. It could be seen that there is an obvious interface between the amorphous and the crystalline regions, and a
6 small amount of medium-range order (MRO) structure could be seen in the amorphous region, which proves that the
7 formation of α -Fe is a spontaneous behavior. The MRO structure was found at the boundary, which also verifies that
8 the process of precipitation α -Fe phase was the combination of medium-range order structures. In the other interface
9 between the crystalline phase (Fe_3B) and the amorphous phase, no obvious boundary and MRO structure were
10 observed. The Fe_3B is a metastable phase, which is the transition structure of the final $\text{M}_{23}(\text{BC})_6$ phase. The
11 amorphous phase still could be found in the crystallization zone. During the manufacturing process of the SLM
12 additive, the large cooling rate is difficult to form a stable remotely ordered structure[50]. In the XRD patterns, the
13 Fe_3B phase was not detected. The $\text{M}_{23}(\text{CB})_6$ phase is formed when the Fe_3B phase reaches a certain concentration[49].
14 The formation of carbides and borides may be due to the formation of the primary α -Fe phase leading to the
15 segregation and aggregation of C and B elements. $\text{M}_{23}(\text{CB})_6$ has a lower enthalpy of formation than other carbides
16 and therefore precipitates preferentially[51]. Previous studies have shown that in amorphous components with high
17 GFA, small atomic sizes C and B have higher crystallization resistance, less prone to diffusion and nucleation[52].
18 This also explains the appearance of $\text{M}_{23}(\text{CB})_6$ as a secondary phase. The different regions of amorphous have
19 different growth mechanisms during the crystallization process[16]. The amorphous phase in the HAZ has
20 prefabricated nucleation points under annealing, so it has lower activation energy for crystallization. The high-
21 resolution images of different crystalline regions show different degrees of confusion, which also confirms this.
22
23
24
25
26
27
28
29
30
31
32
33
34
35
36
37
38
39
40
41
42
43
44
45
46
47

48 3.3 Thermal analysis

49
50
51
52
53
54
55
56
57
58
59
60
61
62
63
64
65

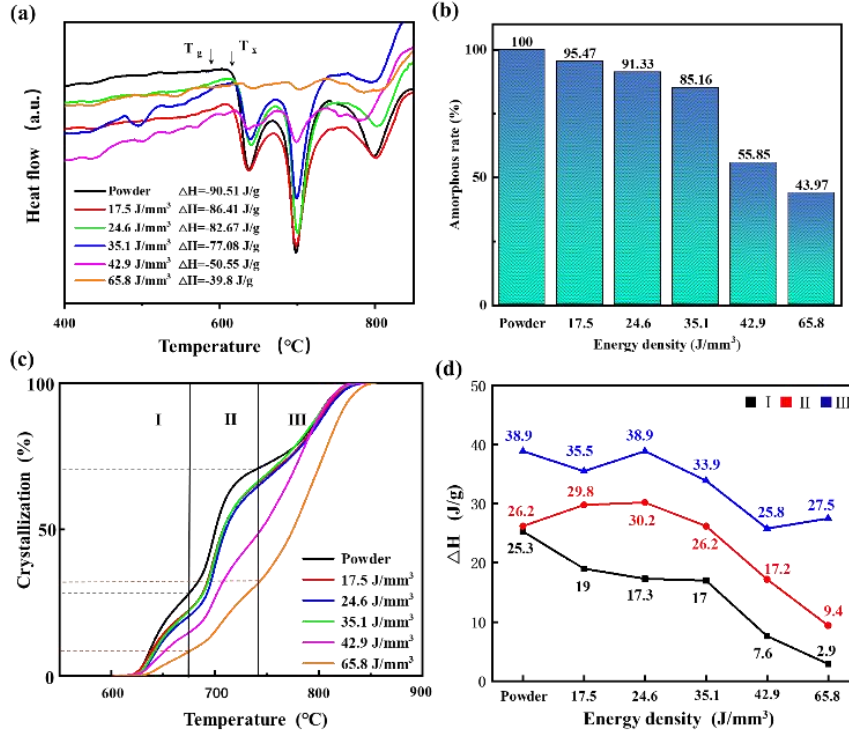


Fig. 8 a) The DSC curves of samples with different energy densities. b) The amorphous rate of samples with different energy densities. c) The crystallization-temperature curves of different samples. d) The ΔH in different crystallization stages.

The DSC curves of the powder and samples with different energy densities are shown in Fig. 8(a). The glass transition temperature T_g of the amorphous is 579°C , and the initial crystallization temperature T_x is 603°C . In order to obtain the amorphous content of the samples, it can be calculated according to the crystallization relaxation enthalpy[10].

$$A = \frac{\Delta H_{\text{Sample}}}{\Delta H_{\text{Powder}}} \times 100\% \quad (3)$$

Where A is the fraction of the amorphous phase, and ΔH_{Sample} and ΔH_{Powder} are the relaxation enthalpies of the as-printed samples and original amorphous powders. According to Eq. (3), the amorphous rate of samples with different energy densities can be calculated (As shown in Fig. 8(b)). The amorphous rate decreased with the increase of energy density, and the highest amorphous content reached 95.47%. When the energy density is lower than 35.1 J/mm^3 , the samples have a high amorphous content. While the energy density is higher than this value, the amorphous rate will be greatly reduced. It can be observed that there are three crystallization processes I, II, and III in the DSC curves. The initial crystallization temperature of I, II, and III is 603°C , 669°C , and 741°C . The crystallization rate and relaxation enthalpies of the specimens differ at different energy densities, but the trend of the DSC curves is consistent.

1 Samples with different amorphous content have the same starting and ending crystallization temperatures at different
 2 stages. As shown in Fig. 8(c), to further analyze the crystallization behavior of the samples with different energy
 3 densities at different stages, the crystallization fraction with temperature changes was calculated by the definite
 4 integral function arithmetic. The crystallization-temperature curves of the samples with energy densities of
 5 17.5J/mm³, 24.6J/mm³, and 35.1J/mm³ almost overlap, which have high amorphous content. The crystallinity curves
 6 of the powder and sample with the energy density of 42.9J/mm³ and 65.8 J/mm³ are quite different from them. With
 7 the energy density increasing (amorphous content decreases), the crystallization process in stage III gradually
 8 becomes the main crystallization method. In the sample with low amorphous content (65.8J/mm³), the crystallization
 9 of stage III occupies 69.1% during the entire crystallization process. The relaxation enthalpies of the specimens with
 10 different energy densities at the three stages are shown in Fig. 8(d). This proves that the crystalline phase of stage III
 11 is not the main product of the SLM-BMG process[53]. To explore the crystallization behavior at different
 12 temperatures. The samples with the energy density of 24.6 J/mm³ were annealed at temperatures of 579°C, 603°C,
 13 669°C and 741°C, and kept at the temperatures for 2h respectively.

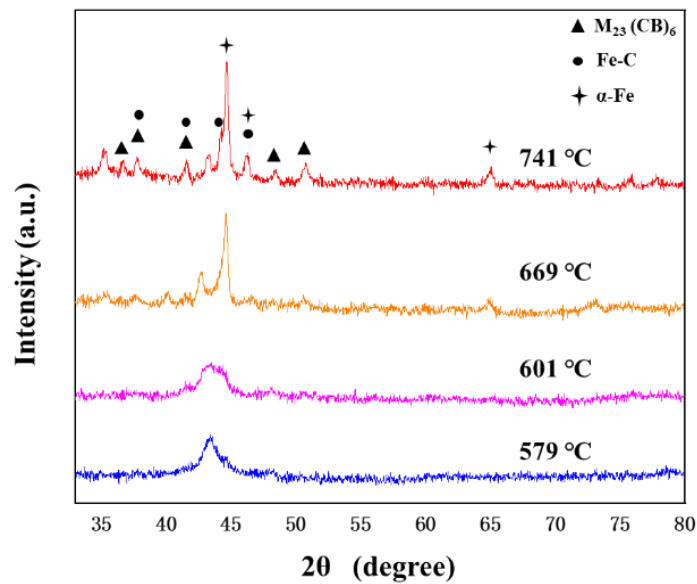


Fig. 9 XRD patterns of samples with 35.1J/mm³ under different heat treatments

55 The XRD patterns of the samples after heat treatment at different temperatures was shown in Fig. 9. With the
 56 increase of heat treatment temperature, the bragger peaks of XRD can be clearly distinguished. The XRD pattern of
 57 the specimen did not change when the heat treatment temperature was 579°C(T_g). The isothermal thermodynamics

1 indicates that nucleation has a higher priority than grain growth. Meanwhile, the driving force contained in the critical
2 thermodynamic condition cannot make the atoms diffuse over long distances to overcome the energy barrier[54]. The
3 XRD pattern of the heat treatment specimen under 601°C(T_x) shows a weak bragger peak at 44°. This phenomenon
4 indicates that the amorphous phase is not stable at this temperature, and there is a tendency to crystallize, but due to
5 the lack of driving force, the crystallization speed is slow[35]. Combined with the XRD pattern and the TEM analysis
6 above, it can be concluded that the primary phase at this temperature is α -Fe. The XRD pattern of the sample after
7 669°C annealings also proved this view. The XRD pattern shows two obvious crystallization peaks, and the main
8 crystalline phase is the α -Fe phase. The bragger peaks of the $M_{23}(CB)_6$ phase were found on the XRD pattern too. It
9 means that the thermodynamic conditions for the formation of $M_{23}(CB)_6$ phase have been satisfied[55]. This
10 phenomenon indicates that the critical temperature of α -Fe phase is lower than that the $M_{23}(CB)_6$ phase. Therefore,
11 under the action of multiple thermal cycles, the grains of α -Fe phase grow and form a sub-micron grain region, which
12 is consistent with the results in Fig. 6(b). After the annealing treatment of 741°C, it can be seen from the XRD pattern
13 that all the amorphous phases in the sample disappear and form the crystalline phase. The crystalline product is
14 mainly α -Fe, $M_{23}(CB)_6$ and Fe-C phase. The formation of the $M_{23}(CB)_6$ phase requires the formation of a long-range
15 ordered structure and the migration and aggregation of the transition phase (Fe_3B) under the action of high
16 temperatures, resulting in the release of lattice stresses[51]. The released stress promotes the formation of nuclei and
17 inhibits grain growth. Meanwhile, under the action of high temperature, some metastable carbides form a stable Fe-
18 C phase.
19
20
21
22
23
24
25
26
27
28
29
30
31
32
33
34
35
36
37
38
39

40 **3.4 Mechanical Properties**

41 The Vickers hardness values for specimens produced by different energy densities were shown in Fig. 10(a). As
42 the energy density increases, the hardness value tends to rise and then fall. The lowest hardness value of 1301 HV
43 was detected on a specimen with an energy density of 17.5 J/mm³. The hardness value of the sample with an energy
44 density of 35.1 J/mm³ reaches the maximum value of 1530HV. When the energy density exceeds 35.1 J/mm³, the
45 hardness of the sample has decreased. As shown in Fig. 4, specimens with an energy density of lower than 35.1
46 J/mm³ have a low level of density, which ensures a large amorphous rate, but the presence of a large number of
47 defects reduces the hardness value of the specimen [43]. The area of HAZ in the sample expands with the increase
48 of energy density. The existence of crystallization phase in the HAZ reduces the hardness value of the sample[39].
49 When the energy density of the specimen is increased from 35.1 J/mm³ to 42.1 J/mm³, the amorphous rate drops from
50
51
52
53
54
55
56
57
58
59
60

85% to 55%.

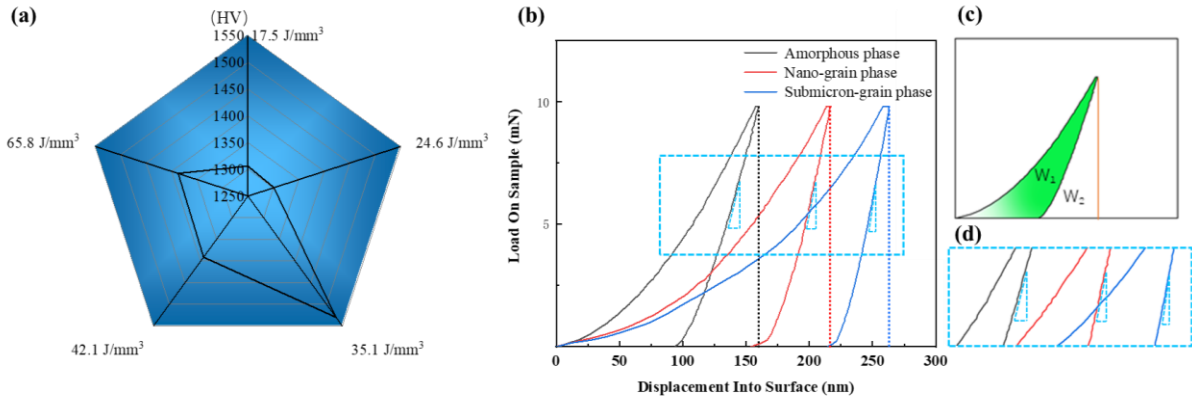


Fig.10 (a) The microhardness of samples with different energy densities. (b) The load-displacement curve of different places. (c) The distribution area of plastic work and elastic work. (d) The local amplification of the load-displacement curve.

In order to further study the influence of crystallization on the hardness of the sample, the part with HAZ was selected from the sample with an energy density of 35.1 J/mm³ to conduct a nanoindentation test. The Fig. 10(b) shows the typical load-displacement curves of different places. The depth of indentation is different under the action of the same load, which proves that the amorphous phase has the highest hardness[56]. As shown in Fig. 10(c), the area of the W₁ region (green area) represents the plastic work and the area of the W₂ region represents the elastic work (white area). The Eq. 4 is used to judge the ductility of the material[57].

$$R = W_1 / (W_1 + W_2) \quad (4)$$

The value of R is used to characterize the ductility of materials, and the big value of R indicates the ductility of the material is better. As shown in Fig. 10 (b), it is obvious that the submicron-grain phase has the best ductility, the ductility of the amorphous phase is the worst. The amorphous phase has no crystal structure and releases stress through the shear bands, while the crystalline phase can release stress through dislocations, thus achieving good ductility[58]. The partial enlargement of Fig. 10(b) is shown in Fig. 10(d). The hypotenuse of the blue triangle is the tangent to the unloading curve at the maximum press-in depth. The hardness of the part can be calculated according to its slope. The calculation method is as follows[59,60]:

$$s = \left. \frac{dP}{dh} \right|_{h_{\max}} \quad (5)$$

Where, S is the contact stiffness, P is the load, and h is the maximum displacement. The value of S is the slope of the hypotenuse of the blue triangle. The contact stiffness of the amorphous phase is minimal (As shown in

Fig.10(d)). The contact stiffness characterizes the ability of a specimen to resist deformation and explains why the amorphous phase is less ductile than the other two phases. Due to the difference in contact stiffness, the contact depth (h_c) of the indentation is not equal to the maximum displacement (h). The relationship between contact depth and maximum displacement is shown in Eq. (6) [61].

$$h_c = h - 0.75P/S \quad (6)$$

From Eq. (6), a large contact stiffness leads to a small contact depth. For the Berkovich indenter, the contact area between the indenter and the specimen can be calculated by Eq. (7).

$$A = 24.56h_c^2 + Ch_c \quad (7)$$

where A is the contact area and C is an empirical constant, generally taken as 150nm for a new indenter. The hardness of a specimen can be calculated according to Eq. (8)[53].

$$H = P/A \quad (8)$$

The hardness of the amorphous, nanocrystalline and submicron phases was calculated to be 18 GPa, 11.05 GPa and 6.99 GPa respectively. To investigate the effect of the crystalline phase on the mechanical properties of SLM-processed samples, nanoindentation tests were conducted in the typical regions. Hardness and Young's modulus maps of the sample with the energy density of 35.1 J/mm³ were shown in Fig. 11.

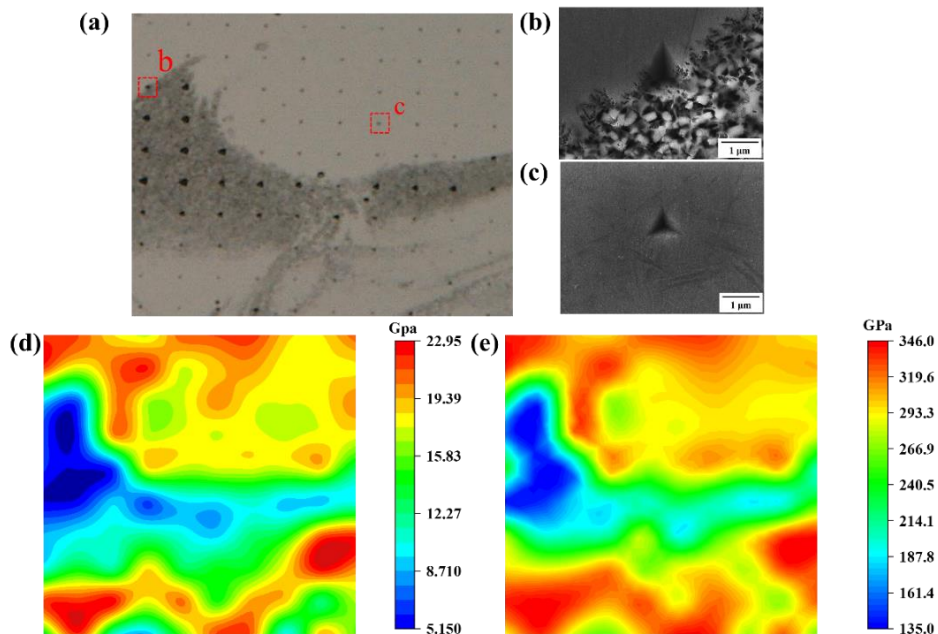


Fig. 11 (a)The 10×10 lattice nanoindentation test result (b) The magnified view of the indentation b. (c) The magnified view of the indentation c. (d) The hardness mapping of 10×10 lattice. (e) The Young's modulus mapping of 10×10 lattice.

1 The position of the nanoindentation of the 10×10 matrix is shown in Fig. 11(a). The distance between each
2 adjacent point is 12 μm. It can be found that the hardness of the HAZ is lower than 12 GPa and the hardness of the
3 molten pool is higher than 17 GPa. The highest hardness in the molten pool reached 22.6 GPa and the average is 15.7
4 GPa. In section 3.2, we explained that the HAZ has been remelted twice, and in the mapping of the nanoindentation
5 hardness distribution, it could be found that the hardness of the region is different from the amorphous region. When
6 the indentation is at the boundary between the crystalline zone and the amorphous zone, the indentation boundary in
7 the crystalline zone shows a camber. This is due to the uneven hardness of the two phases. As can be seen from the
8 mapping in Fig. 11(d), the hardness of specimen shows a sudden drop in the crystalline region. According to the load-
9 displacement curves in Fig. 10(b), the plastic work of the crystalline phase is greater, while the elastic work of the
10 amorphous phase is greater, which means that the amorphous phase will rebound while the crystalline phase will not
11 when unloading the pressure[46]. The comparison between Fig. 11(b) and Fig. 11(c) further illustrates that the
12 hardness of the amorphous phase is much greater than that crystalline phase[56]. The properties of the amorphous
13 phase are not perfectly homogeneous (As shown in Fig. 11(d-e)). The hardness and Young's modulus of material are
14 influenced by the bonding strength and bonding energy of the atoms[55]. The cooling rate during the formation of
15 the amorphous phase is different, which causes a difference in the free volume within the amorphous phase[35]. The
16 amorphous phase is also subjected to multiple thermal cycles during SLM progress. The atoms will migration under
17 the influence of the heat flow[62]. The migration is increased the atomic packing density and reduces the presence
18 of free volume, which significantly increases the hardness of the specimen[55]. Meanwhile, the close packing of
19 atoms also increases the bond strength between the atoms, which increases the Young's modulus of the specimen[63].
20 As shown in Fig. 11 (d-e), there is also a significant difference in hardness and Young's modulus in HAZ. The value
21 of Young's modulus is influenced by the phase composition[64]. According to the above analysis, the nano-grain
22 region was present in the $M_{23}(CB)_6$ phase. The $M_{23}(CB)_6$ phase has a high hardness and high resistance to resist
23 deformation[65]. In the nanocrystalline region, the grains are small and there are a large number of grain boundaries,
24 which will improve the hardness of the sample according to the Hall-Petch formula[66]. In the submicron-grain
25 region, the growth of the grains was severe and the main phase was the α -Fe phase, which has a lower hardness
26 compared with the $M_{23}(CB)_6$ phase[46].
27
28
29
30
31
32
33
34
35
36
37
38
39
40
41
42
43
44
45
46
47
48
49
50
51
52
53
54
55
56
57
58
59
60
61
62
63
64
65

4. Further work

The structure specimen shown in Fig. 12(a) was printed by the energy density of 35.1 J/mm^3 , and the minimum machining unit of the structure was shown in Fig. 12(b). As we could see from the picture, the structural specimen was well formed, which lays the foundation for subsequent dealloying and degradation experiments. The Fig.12(c) and Fig.12(d) were shown the SEM image of the sample. The specimens were placed in H_2SO_4 solution for 6h dealloying. The Fig.12(e) and Fig.12(f) were shown the different morphologies after dealloying. According to the previous analysis of the morphology and structure, the formation of this difference is mainly caused by different crystalline phases. Fig. 12(e) shows the morphology of the nano-grain region after dealloying, and Fig. 12(f) shows the morphology of the submicron-grain region after dealloying. In the H_2SO_4 solution, the α -Fe phase, amorphous phase, and other phases form a tiny galvanic cell. Due to the higher activity of the α -Fe phase, it will be preferentially corroded as a sacrificial anode[67].

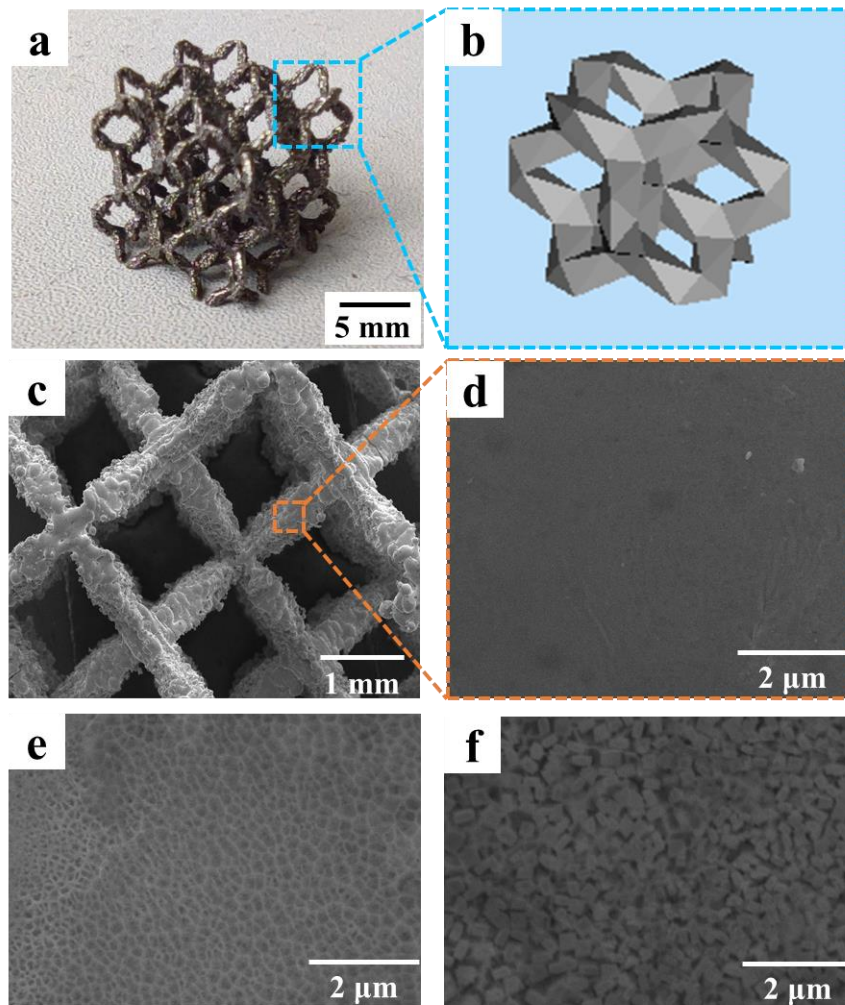


Fig.12 (a) The macro picture of amorphous structural parts; (b) The minimum machining unit for structural parts; (c) The macro

SEM image of sample; (d) The local enlarged SEM image of amorphous structure surface; (e) The morphology of the nano-grain region after dealloying; (f) the morphology of the submicron-grain region after dealloying

As shown in Fig. 13(a), the degradation results of the structural sample after standing in methyl orange for 30 minutes. It is found that the degradation effect of the sample after the dealloying treatment is much better than that of the untreated sample during the same time. There is a small amount of solid phase in the untreated sample (Fig.13(b)), while there is a more solid phase on the surface of the dealloyed sample (Fig.13(c-d)). The nanopores produced on the surface of the dealloyed specimen increase the specific surface area [68]. On the one hand, the pores were conducive to the adsorption of azo dye macromolecules, on the other hand, the corrosion of the α -Fe phase exposes more amorphous components to the solution [69]. The degradation mechanism of amorphous is mainly due to the oxidation-reduction reaction between the Fe^0 in the amorphous and the dye [70]. The azo bond(N=N) breaks and reduces to small molecules, while the solution fades. Fe^0 will be oxidized to Fe^{2+} and Fe^{3+} to form precipitates. Therefore, the more attached area has a better degradation effect. Different surface nanostructures have different effects on the degradation of azo dyes [71]. Uniform nanostructures (Fig.13(c)) have more surface attachments than submicron structures (Fig.13(d)).

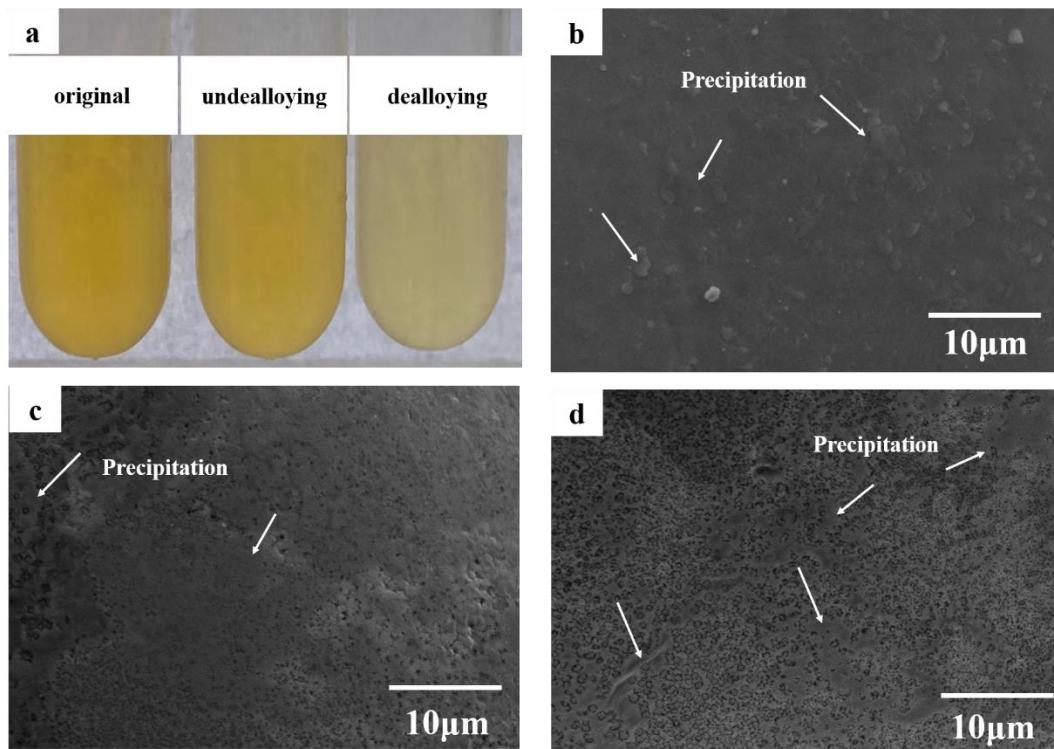


Fig.13 (a) The results of degradation; (b) The SEM image of the non-dealloying sample after degradation; (c)(d) The SEM of dealloying sample after degradation.

5. Conclusion

The FeCrMoWMnSiBC BMG parts were fabricated by SLM technique. The effects of process parameters on the forming, crystallization behavior and mechanical properties of BMG samples were studied. The conclusions were drawn as follow:

- The energy density is the key factor to determine the surface forming condition of the sample. The sample with an energy density greater than 35.1 J/mm^3 is difficult to form, and the RD of the sample with an energy density less than 35.1 J/mm^3 decreases significantly.
- The energy density of 35.1 J/mm^3 is the key parameter for good formation, and the Fe-based BMG parts produced by SLM could achieve a RD of over 95% while maintaining a high amorphous rate ($> 95.47\%$).
- The amorphous rate in the specimen decreases significantly when the energy density is greater than 35.1 J/mm^3 . The $\alpha\text{-Fe}$ and $\text{M}_{23}(\text{CB})_6$ are the main crystalline phases in the production of Fe-based metallic glass by SLM, and the crystallization mainly occurs in the heat-affected zone.
- The HAZ shows obvious structural differences under the effect of complex thermal cycles, and the differences are mainly reflected in the size of the crystalline phase
- The weak area mainly appeared in the HAZ, and the highest nanoindentation strength in the molten pool reached 22.6 GPa. The concentration of free volume of the amorphous phase is not uniform, and a high concentration of free volume will significantly reduce the hardness of the sample.
- The sample after dealloying has a great degradation effect.

Acknowledgments

This research was supported by Natural Science Foundation of China (52075317), the Royal Society through International Exchanges 2018 Cost Share (China) scheme (IEC\NSFC\181278), Shanghai Science and Technology Committee Innovation Grant (19511106400, 19511106402), Shanghai Local Colleges and Universities Capacity Building Special Plan Project (19030501300).

References

- [1] H.Y. Jung, S.J. Choi, K.G. Prashanth, M. Stoica, S. Scudino, S. Yi, U. Kühn, D.H. Kim, K.B. Kim, J. Eckert, Fabrication of Fe-based bulk metallic glass by selective laser melting: A parameter study, *Mater. Des.* 86 (2015) 703–708. <https://doi.org/10.1016/J.MATDES.2015.07.145>.
- [2] N. Li, J. Zhang, W. Xing, D. Ouyang, L. Liu, 3D printing of Fe-based bulk metallic glass composites with combined high strength and fracture toughness, *Mater. Des.* 143 (2018) 285–296. <https://doi.org/10.1016/j.matdes.2018.01.061>.
- [3] Z. Mahbooba, L. Thorsson, M. Unosson, P. Skoglund, H. West, T. Horn, C. Rock, E. Vogli, O. Harrysson, Additive manufacturing of an iron-based bulk metallic glass larger than the critical casting thickness, *Appl. Mater. Today*. 11 (2018) 264–269. <https://doi.org/10.1016/J.APMT.2018.02.011>.
- [4] X.D. Nong, X.L. Zhou, Y.X. Ren, Fabrication and characterization of Fe-based metallic glasses by Selective Laser Melting, *Opt. Laser Technol.* 109 (2019) 20–26. <https://doi.org/10.1016/J.OPTLASTEC.2018.07.059>.
- [5] D. Ouyang, N. Li, W. Xing, J. Zhang, L. Liu, 3D printing of crack-free high strength Zr-based bulk metallic glass composite by selective laser melting, *Intermetallics*. 90 (2017) 128–134. <https://doi.org/10.1016/j.intermet.2017.07.010>.
- [6] W. Liang, Z. Ning, Z. Dang, L. Wu, Plastic deformation behaviors of Ni- and Zr-based bulk metallic glasses subjected to nanoindentation, *Mater. Charact.* 86 (2013) 290–295. <https://doi.org/10.1016/j.matchar.2013.10.014>.
- [7] X.P. Li, C.W. Kang, H. Huang, L.C. Zhang, T.B. Sercombe, Selective laser melting of an Al₈₆Ni₆Y_{4.5}Co₂La_{1.5} metallic glass: Processing, microstructure evolution and mechanical properties, *Mater. Sci. Eng. A*. 606 (2014) 370–379. <https://doi.org/10.1016/j.msea.2014.03.097>.
- [8] L. Deng, S. Wang, P. Wang, U. Kühn, S. Pauly, Selective laser melting of a Ti-based bulk metallic glass, *Mater. Lett.* 212 (2018) 346–349. <https://doi.org/10.1016/j.matlet.2017.10.130>.
- [9] X. Gao, X. Lin, J. Yu, Y. Li, Y. Hu, W. Fan, S. Shi, W. Huang, Selective Laser Melting (SLM) of in-situ beta phase reinforced Ti/Zr-based bulk metallic glass matrix composite, *Scr. Mater.* 171 (2019) 21–25. <https://doi.org/10.1016/j.scriptamat.2019.06.007>.
- [10] D. Ouyang, W. Xing, N. Li, Y. Li, L. Liu, Structural evolutions in 3D-printed Fe-based metallic glass fabricated by selective laser melting, *Addit. Manuf.* 23 (2018) 246–252. <https://doi.org/10.1016/j.addma.2018.08.020>.
- [11] L. Wang, H. Wang, Y. Liu, Z. Fu, T. Peng, J. Shen, S. Zhou, M. Yan, G. Wang, Y. Dai, Selective laser melting helps fabricate record-large bulk metallic glass: Experiments, simulation and demonstrative part, *J. Alloys*

- 1
2
3
4
5
6
7
8
9
10
11
12
13
14
15
16
17
18
19
20
21
22
23
24
25
26
27
28
29
30
31
32
33
34
35
36
37
38
39
40
41
42
43
44
45
46
47
48
49
50
51
52
53
54
55
56
57
58
59
60
61
62
63
64
65
- Compd. 808 (2019). <https://doi.org/10.1016/j.jallcom.2019.151731>.
- [12] Ł. Żrodowski, B. Wysocki, R. Wróblewski, K.J. Kurzydłowski, W. Świąszkowski, The Novel Scanning Strategy For Fabrication Metallic Glasses By Selective Laser Melting, *Fraunhofer Direct Digit. Manuf. Conf. (DDMC 2016)*. (2016) 1–6.
- [13] Q. Jiang, P. Zhang, Z. Yu, H. Shi, D. Wu, H. Yan, X. Ye, Q. Lu, Y. Tian, A Review on Additive Manufacturing of Pure Copper, *Coatings*. 11 (2021) 740. <https://doi.org/10.3390/coatings11060740>.
- [14] Q. Jiang, P. Zhang, Z. Yu, Y. Tian, S. Ma, AlCoCrFeNi high entropy alloy fabricated via selective laser melting reinforced by Fe-based metallic glass, *Mater. Lett.* (2021) 130994. <https://doi.org/10.1016/j.matlet.2021.130994>.
- [15] X.P. Li, M.P. Roberts, S. O’Keeffe, T.B. Sercombe, Selective laser melting of Zr-based bulk metallic glasses: Processing, microstructure and mechanical properties, *Mater. Des.* 112 (2016) 217–226. <https://doi.org/10.1016/J.MATDES.2016.09.071>.
- [16] D. Ouyang, N. Li, L. Liu, Structural heterogeneity in 3D printed Zr-based bulk metallic glass by selective laser melting, *J. Alloys Compd.* 740 (2018) 603–609. <https://doi.org/10.1016/j.jallcom.2018.01.037>.
- [17] V. Pacheco, D. Karlsson, J.J. Marattukalam, M. Stolpe, B. Hjörvarsson, U. Jansson, M. Sahlberg, Thermal stability and crystallization of a Zr-based metallic glass produced by suction casting and selective laser melting, *J. Alloys Compd.* 825 (2020). <https://doi.org/10.1016/j.jallcom.2020.153995>.
- [18] Y.M. Zou, Y.S. Wu, K.F. Li, C.L. Tan, Z.G. Qiu, D.C. Zeng, Selective laser melting of crack-free Fe-based bulk metallic glass via chessboard scanning strategy, *Mater. Lett.* 272 (2020) 2–5. <https://doi.org/10.1016/j.matlet.2020.127824>.
- [19] P. Zhang, J. Tan, Y. Tian, H. Yan, Z. Yu, Research progress on selective laser melting (SLM) of bulk metallic glasses (BMGs): a review, *Int. J. Adv. Manuf. Technol.* (2021). <https://doi.org/10.1007/s00170-021-07990-8>.
- [20] N. Luo, C. Scheitler, N. Ciftci, F. Galgon, Z. Fu, V. Uhlenwinkel, M. Schmidt, C. Körner, Preparation of Fe-Co-B-Si-Nb bulk metallic glasses by laser powder bed fusion: Microstructure and properties, *Mater. Charact.* 162 (2020) 110206. <https://doi.org/10.1016/j.matchar.2020.110206>.
- [21] H.X. Li, J.E. Gao, Z.B. Jiao, Y. Wu, Z.P. Lu, Glass-forming ability enhanced by proper additions of oxygen in a Fe-based bulk metallic glass, *Appl. Phys. Lett.* 95 (2009) 161905. <https://doi.org/10.1063/1.3248186>.
- [22] F. Xie, Q. Chen, J. Gao, Y. Li, Laser 3D Printing of Fe-Based Bulk Metallic Glass: Microstructure Evolution and Crack Propagation, *J. Mater. Eng. Perform.* 28 (2019) 3478–3486. <https://doi.org/10.1007/s11665-019-04103-1>.
- [23] S. Pauly, L. Löber, R. Petters, M. Stoica, S. Scudino, U. Kühn, J. Eckert, Processing metallic glasses by selective

- 1 laser melting, *Mater. Today*. 16 (2013) 37–41. <https://doi.org/10.1016/j.mattod.2013.01.018>.
- 2 [24] C. Yang, C. Zhang, L. Liu, Excellent degradation performance of 3D hierarchical nanoporous structures of
3 copper towards organic pollutants, *J. Mater. Chem. A*. 6 (2018) 20992–21002.
4
5 <https://doi.org/10.1039/C8TA07973K>.
- 6 [25] P. Zhang, H. Yan, C. Yao, Z. Li, Z. Yu, P. Xu, Synthesis of Fe-Ni-B-Si-Nb amorphous and crystalline composite
7 coatings by laser cladding and remelting, *Surf. Coatings Technol.* 206 (2011) 1229–1236.
8
9 <https://doi.org/10.1016/j.surfcoat.2011.08.039>.
- 10 [26] P. Zhang, H. Yan, P. Xu, Z. Yu, C. Li, Microstructure and tribological behavior of amorphous and crystalline
11 composite coatings using laser melting, *Appl. Surf. Sci.* 258 (2012) 6902–6908.
12
13 <https://doi.org/10.1016/j.apsusc.2012.03.130>.
- 14 [27] R. Li, Z. Li, J. Huang, P. Zhang, Y. Zhu, Effect of Ni-to-Fe ratio on structure and properties of Ni-Fe-B-Si-Nb
15 coatings fabricated by laser processing, *Appl. Surf. Sci.* 257 (2011) 3554–3557.
16
17 <https://doi.org/10.1016/j.apsusc.2010.11.073>.
- 18 [28] P. Zhang, H. Yan, P. Xu, Q. Lu, C. Li, Z. Yu, Influence of different annealing temperatures and cooling rates on
19 amorphous and crystalline composite coating, *Surf. Coatings Technol.* 206 (2012) 4981–4987.
20
21 <https://doi.org/10.1016/j.surfcoat.2012.05.142>.
- 22 [29] P. Zhang, H. Yan, C. Yao, Z. Li, Z. Yu, P. Xu, Relationship between the γ and some parameters of Fe-based bulk
23 metallic glasses, *Int. J. Mater. Res.* 103 (2012) 336–340. <https://doi.org/10.3139/146.110649>.
- 24 [30] Q. Zhang, P. Zhang, H. Yan, Z. Yu, D. Wu, H. Shi, S. Li, Y. Tian, Magnetic-field-assisted laser cladding in the
25 preparation of a crack-free Fe-Cr-Mo-C-Y-B amorphous coating on steel, *Philos. Mag. Lett.* 100 (2020) 86–93.
26
27 <https://doi.org/10.1080/09500839.2020.1725245>.
- 28 [31] A. Simchi, H. Pohl, Effects of laser sintering processing parameters on the microstructure and densification of
29 iron powder, *Mater. Sci. Eng. A*. (2003). [https://doi.org/10.1016/S0921-5093\(03\)00341-1](https://doi.org/10.1016/S0921-5093(03)00341-1).
- 30 [32] J. Bi, Z. Lei, Y. Chen, X. Chen, X. Qin, Z. Tian, Effect of process parameters on formability and surface quality
31 of selective laser melted Al-Zn-Sc-Zr alloy from single track to block specimen, *Opt. Laser Technol.* 118 (2019)
32 132–139. <https://doi.org/10.1016/j.optlastec.2019.05.008>.
- 33 [33] M. Boutaous, X. Liu, D.A. Siginer, S. Xin, Balling phenomenon in metallic laser based 3D printing process, *Int.*
34 *J. Therm. Sci.* 167 (2021) 107011. <https://doi.org/10.1016/j.ijthermalsci.2021.107011>.
- 35 [34] F. Cabanettes, A. Joubert, G. Chardon, V. Dumas, J. Rech, C. Grosjean, Z. Dimkovski, Topography of as built
36
37
38
39
40
41
42
43
44
45
46
47
48
49
50
51
52
53
54
55
56
57
58
59
60
61
62
63
64
65

1 surfaces generated in metal additive manufacturing: A multi scale analysis from form to roughness, *Precis. Eng.*
2 52 (2018) 249–265. <https://doi.org/10.1016/j.precisioneng.2018.01.002>.

- 3
4 [35] X.P. Li, C.W. Kang, H. Huang, T.B. Sercombe, The role of a low-energy-density re-scan in fabricating crack-
5 free Al85Ni5Y6Co2Fe2 bulk metallic glass composites via selective laser melting, *Mater. Des.* 63 (2014) 407–
6 411. <https://doi.org/10.1016/j.matdes.2014.06.022>.
- 7
8 [36] A.F. de Souza, K.S. Al-Rubaie, S. Marques, B. Zluhan, E.C. Santos, Effect of laser speed, layer thickness, and
9 part position on the mechanical properties of maraging 300 parts manufactured by selective laser melting, *Mater.*
10 *Sci. Eng. A.* 767 (2019) 138425. <https://doi.org/10.1016/j.msea.2019.138425>.
- 11
12 [37] L. Mugwagwa, D. Dimitrov, S. Matope, I. Yadroitsev, Influence of process parameters on residual stress related
13 distortions in selective laser melting, *Procedia Manuf.* 21 (2018) 92–99.
14
15 <https://doi.org/10.1016/j.promfg.2018.02.099>.
- 16
17 [38] T. Zakrzewski, J. Kozak, M. Witt, M. Debowska-Wasak, Dimensional analysis of the effect of SLM parameters
18 on surface roughness and material density, *Procedia CIRP.* 95 (2020) 115–120.
19
20 <https://doi.org/10.1016/j.procir.2020.01.182>.
- 21
22 [39] D.C. Hofmann, P. Bordeenithikasem, A. Pate, S.N. Roberts, E. Vogli, Developing Processing Parameters and
23 Characterizing Microstructure and Properties of an Additively Manufactured FeCrMoBC Metallic Glass Forming
24 Alloy, *Adv. Eng. Mater.* 20 (2018). <https://doi.org/10.1002/adem.201800433>.
- 25
26 [40] X. Tang, S. Zhang, C. Zhang, J. Chen, J. Zhang, Y. Liu, Optimization of laser energy density and scanning
27 strategy on the forming quality of 24CrNiMo low alloy steel manufactured by SLM, *Mater. Charact.* 170 (2020)
28 110718. <https://doi.org/10.1016/j.matchar.2020.110718>.
- 29
30 [41] S. Katakam, J.Y. Hwang, S. Paital, R. Banerjee, H. Vora, N.B. Dahotre, In situ laser synthesis of Fe-based
31 amorphous matrix composite coating on structural steel, *Metall. Mater. Trans. A Phys. Metall. Mater. Sci.* 43
32 (2012) 4957–4966. <https://doi.org/10.1007/s11661-012-1312-4>.
- 33
34 [42] Y. Lu, Y. Huang, J. Wu, X. Lu, Z. Qin, D. Daisenberger, Y.L. Chiu, Graded structure of laser direct
35 manufacturing bulk metallic glass, *Intermetallics.* 103 (2018) 67–71.
36
37 <https://doi.org/10.1016/j.intermet.2018.10.005>.
- 38
39 [43] C. Qiu, C. Panwisawas, M. Ward, H.C. Basoalto, J.W. Brooks, M.M. Attallah, On the role of melt flow into the
40 surface structure and porosity development during selective laser melting, *Acta Mater.* 96 (2015) 72–79.
41
42 <https://doi.org/10.1016/j.actamat.2015.06.004>.
- 43
44
45
46
47
48
49
50
51
52
53
54
55
56
57
58
59
60
61
62
63
64
65

- 1 [44] T.A.C.M. van der Put, Theoretical derivation of the WLF- and annealing equations, *J. Non. Cryst. Solids*. 356
2 (2010) 394–399. <https://doi.org/10.1016/j.jnoncrysol.2009.11.031>.
3
- 4 [45] W.M. Steen, *Laser Material Processing*, 2003. <https://doi.org/10.1007/978-1-4471-3752-8>.
5
- 6 [46] H.X. Li, Z.C. Lu, S.L. Wang, Y. Wu, Z.P. Lu, Fe-based bulk metallic glasses: Glass formation, fabrication,
7 properties and applications, *Prog. Mater. Sci.* 103 (2019) 235–318.
8
9 <https://doi.org/10.1016/j.pmatsci.2019.01.003>.
- 10 [47] O.A. Graeve, M.S. Saterlie, R. Kanakala, S.D. De La Torre, J.C. Farmer, The kinetics of devitrification of
11 amorphous alloys: The time-temperature-crystallinity diagram describing the spark plasma sintering of Fe-based
12 metallic glasses, *Scr. Mater.* (2013). <https://doi.org/10.1016/j.scriptamat.2013.02.019>.
13
14
15
16
17
18 [48] A. Hirata, Y. Hirotsu, E. Matsubara, T. Ohkubo, K. Hono, Mechanism of nanocrystalline microstructure
19 formation in amorphous Fe-Nb-B alloys, *Phys. Rev. B - Condens. Matter Mater. Phys.* (2006).
20
21 <https://doi.org/10.1103/PhysRevB.74.184204>.
22
23
24 [49] L. Kaufman, J.H. Perepezko, K. Hildal, J. Farmer, D. Day, N. Yang, D. Branagan, Transformation, stability and
25 Pourbaix diagrams of high performance corrosion resistant (HPCRM) alloys, *Calphad Comput. Coupling Phase*
26 *Diagrams Thermochem.* (2009). <https://doi.org/10.1016/j.calphad.2008.09.019>.
27
28
29
30 [50] V.K. Balla, A. Bandyopadhyay, Laser processing of Fe-based bulk amorphous alloy, *Surf. Coatings Technol.*
31 (2010). <https://doi.org/10.1016/j.surfcoat.2010.10.029>.
32
33
34 [51] M.J. Duarte, A. Kostka, D. Crespo, J.A. Jimenez, A.C. Dippel, F.U. Renner, G. Dehm, Kinetics and
35 crystallization path of a Fe-based metallic glass alloy, *Acta Mater.* (2017).
36
37 <https://doi.org/10.1016/j.actamat.2017.01.031>.
38
39
40 [52] Y. Wu, X.D. Hui, Z.P. Lu, Z.Y. Liu, L. Liang, G.L. Chen, Effects of metalloids elements on the glass-forming
41 ability of Fe-based alloys, *J. Alloys Compd.* (2009). <https://doi.org/10.1016/j.jallcom.2007.12.002>.
42
43
44 [53] X. Lu, M. Nursulton, Y. Du, W. Liao, Structural and mechanical characteristics of Cu₅₀Zr₄₃Al₇ bulk metallic
45 glass fabricated by selective laser melting, *Materials (Basel)*. 12 (2019). <https://doi.org/10.3390/ma12050775>.
46
47
48 [54] H. Yao, L. Wang, Z. Zhou, B. Wang, Z. Tan, D. He, Y. Xue, Thermal transport property correlated with
49 microstructural evolution of Fe-based amorphous alloy, *Acta Mater.* (2020).
50
51 <https://doi.org/10.1016/j.actamat.2020.09.072>.
52
53
54 [55] N. Luo, C. Scheitler, N. Ciftci, F. Galgon, Z. Fu, V. Uhlenwinkel, M. Schmidt, C. Körner, Preparation of Fe-Co-
55 B-Si-Nb bulk metallic glasses by laser powder bed fusion: Microstructure and properties, *Mater. Charact.* 162
56
57
58
59
60
61
62
63
64
65

(2020) 110206. <https://doi.org/10.1016/j.matchar.2020.110206>.

- [56] X.J. Shen, C. Zhang, Y.G. Yang, L. Liu, On the microstructure, mechanical properties and wear resistance of an additively manufactured Ti64/metallic glass composite, *Addit. Manuf.* 25 (2019) 499–510. <https://doi.org/10.1016/j.addma.2018.12.006>.
- [57] T. Yang, S. Xia, S. Liu, C. Wang, S. Liu, Y. Zhang, J. Xue, S. Yan, Y. Wang, Effects of AL addition on microstructure and mechanical properties of Al_xCoCrFeNi High-entropy alloy, *Mater. Sci. Eng. A.* 648 (2015) 15–22. <https://doi.org/10.1016/j.msea.2015.09.034>.
- [58] P. Gong, G. Yin, Z. Jamili-Shirvan, H. Ding, X. Wang, J. Jin, Influence of deep cryogenic cycling on the rejuvenation and plasticization of TiZrHfBeCu high-entropy bulk metallic glass, *Mater. Sci. Eng. A.* 797 (2020) 140078. <https://doi.org/10.1016/j.msea.2020.140078>.
- [59] G.M. Pharr, W.C. Oliver, Measurement of hardness and elastic modulus by instrumented indentation: Advances in understanding and refinements to methodology, *J. Mater. Res.* 19 (2004) 3–20.
- [60] X. Wei, P. Zhang, Z. Yu, H. Yan, D. Wu, H. Shi, J. Chen, Q. Lu, Y. Tian, S. Ma, W. Lei, Effect of phase transformation on mechanical properties of Al_{16.80}Co_{20.74}Cr_{20.49}Fe_{21.28}Ni_{20.70} high entropy alloy coatings processed by laser cladding, *J. Alloys Compd.* 862 (2021). <https://doi.org/10.1016/j.jallcom.2020.158563>.
- [61] Y.W. Bao, W. Wang, Y.C. Zhou, Investigation of the relationship between elastic modulus and hardness based on depth-sensing indentation measurements, *Acta Mater.* 52 (2004) 5397–5404. <https://doi.org/10.1016/j.actamat.2004.08.002>.
- [62] Q. Zhou, Y. Du, Q. Jia, W. Han, X. Zhao, Y. Deng, H. Wang, A nanoindentation study of Ti-based high entropy bulk metallic glasses at elevated temperatures, *J. Non. Cryst. Solids.* 532 (2020) 119878. <https://doi.org/10.1016/j.jnoncrysol.2019.119878>.
- [63] X. Wang, P. Gong, L. Deng, J. Jin, S. Wang, P. Zhou, Nanoindentation study on the room temperature creep characteristics of a senary Ti_{16.7}Zr_{16.7}Hf_{16.7}Cu_{16.7}Ni_{16.7}Be_{16.7} high entropy bulk metallic glass, *J. Non. Cryst. Solids.* 470 (2017) 27–37. <https://doi.org/10.1016/j.jnoncrysol.2017.04.041>.
- [64] P.D. Niu, R.D. Li, T.C. Yuan, S.Y. Zhu, C. Chen, M.B. Wang, L. Huang, Microstructures and properties of an equimolar AlCoCrFeNi high entropy alloy printed by selective laser melting, *Intermetallics.* 104 (2019) 24–32. <https://doi.org/10.1016/j.intermet.2018.10.018>.
- [65] R. Zhou, Y. Liu, B. Liu, J. Li, Q. Fang, Precipitation behavior of selective laser melted FeCoCrNi_{0.05} high entropy alloy, *Intermetallics.* 106 (2019) 20–25. <https://doi.org/10.1016/j.intermet.2018.12.001>.

- 1 [66] Q. Jiang, P. Zhang, Z. Yu, H. Shi, S. Li, D. Wu, H. Yan, X. Ye, J. Chen, Microstructure and Mechanical
2 Properties of Thick-Walled Inconel 625 Alloy Manufactured by Wire Arc Additive Manufacture with Different
3 Torch Paths, *Adv. Eng. Mater.* (2020). <https://doi.org/10.1002/adem.202000728>.
4
5
6 [67] S.X. Liang, X. Wang, W. Zhang, Y.J. Liu, W. Wang, L.C. Zhang, Selective laser melting manufactured porous
7 Fe-based metallic glass matrix composite with remarkable catalytic activity and reusability, *Appl. Mater. Today*.
8 19 (2020) 100543. <https://doi.org/10.1016/j.apmt.2019.100543>.
9
10
11 [68] C.Q. Zhang, Z.W. Zhu, H.F. Zhang, Z.Q. Hu, Rapid reductive degradation of azo dyes by a unique structure of
12 amorphous alloys, *Chinese Sci. Bull.* 56 (2011) 3988–3992. <https://doi.org/10.1007/s11434-011-4781-8>.
13
14
15 [69] C. Zhang, Z. Zhu, H. Zhang, Z. Hu, On the decolorization property of Fe-Mo-Si-B alloys with different
16 structures, *J. Non. Cryst. Solids.* 358 (2012) 61–64. <https://doi.org/10.1016/j.jnoncrysol.2011.08.023>.
17
18
19 [70] S.X. Liang, W. Zhang, W. Wang, G. Jia, W. Yang, L.C. Zhang, Surface reactivation of FeNiPC metallic glass: A
20 strategy for highly enhanced catalytic behavior, *J. Phys. Chem. Solids.* 132 (2019) 89–98.
21
22
23 <https://doi.org/10.1016/j.jpccs.2019.04.022>.
24
25
26 [71] C. Zhang, Z. Zhu, H. Zhang, Effects of the addition of Co, Ni or Cr on the decolorization properties of Fe-Si-B
27 amorphous alloys, *J. Phys. Chem. Solids.* 110 (2017) 152–160. <https://doi.org/10.1016/j.jpccs.2017.06.010>.
28
29
30
31
32
33
34
35
36
37
38
39
40
41
42
43
44
45
46
47
48
49
50
51
52
53
54
55
56
57
58
59
60
61
62
63
64
65